AGU PUBLICATIONS

JGR

Journal of Geophysical Research: Solid Earth

RESEARCH ARTICLE

10.1002/2014JB011186

Key Points:
- Brittle creep occurs in porous limestone
- Subcritical cracking is dominant at high stress and low confining pressure
- A switch in deformation mechanism is observed at low creep strain rate

Correspondence to:
N. Brantut,
n.brantut@ucl.ac.uk

Citation:
Brantut, N., M. J. Heap, P. Baud, and P. G. Meredith (2014), Mechanisms of time-dependent deformation in porous limestone, *J. Geophys. Res. Solid Earth*, *119*, 5444–5463, doi:10.1002/2014JB011186.

Received 11 APR 2014
Accepted 28 JUN 2014
Accepted article online 1 JUL 2014
Published online 25 JUL 2014

Mechanisms of time-dependent deformation in porous limestone

Nicolas Brantut[1], Michael J. Heap[2], Patrick Baud[2], and Philip G. Meredith[1]

[1]Rock and Ice Physics Laboratory, Department of Earth Sciences, University College London, London, UK, [2]Laboratoire de Déformation des Roches, Géophysique Expérimentale, Institut de Physique de Globe de Strasbourg (UMR 7516 CNRS, Université de Strasbourg/EOST), Strasbourg, France

Abstract We performed triaxial deformation experiments on a water-saturated porous limestone under constant strain rate and constant stress (creep) conditions. The tests were conducted at room temperature and at low effective pressures P_{eff}=10 and P_{eff}=20 MPa, in a regime where the rock is nominally brittle when tested at a constant strain rate of 10^{-5} s^{-1}. Under these conditions and at constant stress, the phenomenon of brittle creep occurs. At P_{eff}=10 MPa, brittle creep follows similar trends as those observed in other rock types (e.g., sandstones and granites): only small strains are accumulated before failure, and damage accumulation with increasing strain (as monitored by *P* wave speeds measurements during the tests) is not strongly dependent on the applied stresses. At P_{eff}=20 MPa, brittle creep is also macroscopically observed, but when the creep strain rate is lower than $\approx 10^{-7}$ s^{-1}, we observe that (1) much larger strains are accumulated, (2) less damage is accumulated with increasing strain, and (3) the deformation tends to be more compactant. These observations can be understood by considering that another deformation mechanism, different from crack growth, is active at low strain rates. We explore this possibility by constructing a deformation mechanism map that includes both subcritical crack growth and pressure solution creep processes; the increasing contribution of pressure solution creep at low strain rates is consistent with our observations.

1. Introduction

Limestones constitute a major element of the sedimentary cover worldwide [*Ford and Williams*, 2007] and are thus subject to the deformation and fluid flow processes occurring in the upper crust. Field evidence for brittle and ductile deformation are observed, often in close association, in limestone formations [e.g., *Gratier and Gamond*, 1990]: they host active faults (e.g., in the Italian Apenines [e.g., *Tesei et al.*, 2013] and in the gulf of Corinth [e.g., *Bastesen et al.*, 2009]) and folds (e.g., in the Subalpine Chains of the Alps [e.g., *Linzer et al.*, 1995]) and are also a major reservoir rock hosting aquifers and hydrocarbon reserves. The mechanical behavior of limestones has hence an important impact on the dynamics of the upper crust and on the response of natural aquifers and reservoirs to changes in stress.

It is well established experimentally that porous limestones, similarly to other porous rocks, behave in a brittle manner at low confining pressure but become ductile with increasing confining pressure [e.g., *Baud et al.*, 2000; *Wong and Baud*, 2012]. The brittle regime in such rocks is characterized by the occurrence of dilatancy and the formation of a macroscopic shear fault associated with a significant strength loss [*Paterson and Wong*, 2005]. These features (common to all brittle rocks) can be explained by the growth of tensile microcracks originating from local stress concentrations, such as preexisting pores [*Wong and Baud*, 2012]. By contrast, the ductile regime is characterized by the occurrence of inelastic compaction, distributed deformation, and strain hardening [e.g., *Baud et al.*, 2000; *Vajdova et al.*, 2004]. Under dry conditions, inelastic compaction in limestone originates not only from pore collapse promoted by microcracking but also by intracrystalline plasticity of the calcite grains [*Baud et al.*, 2000; *Zhu et al.*, 2010]. Intracrystalline plastic deformation mechanisms are indeed active in calcite at room temperature [e.g., *Turner et al.*, 1954] and likely occur in the macroscopically brittle (dilatant) regime as well as the ductile (compactant) regime [e.g., *Fredrich et al.*, 1989], unlike most other rock-forming minerals found in porous sandstones, such as quartz or feldspar, which remain purely brittle at room temperature. The transition pressure between the brittle and ductile regimes is generally found to be a function of the initial porosity of the rock, as well as factors such as pore size and the partitioning between micropores and macropores, with higher porosities and larger pores promoting lower transition pressures [*Wong and Baud*, 2012].

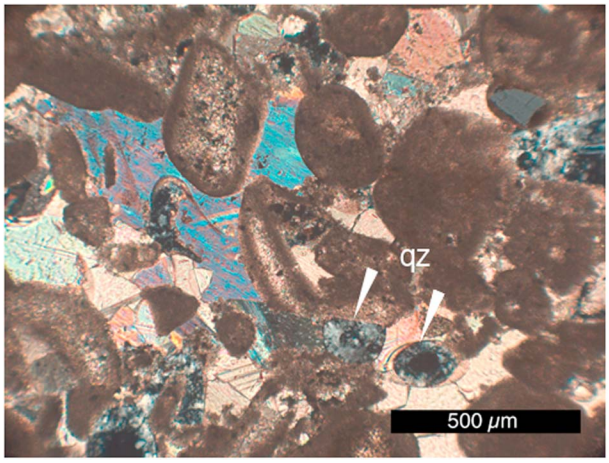

Figure 1. Micrograph of a thin section of intact Pond freestone Purbeck limestone sample, under crossed polars. The white arrows indicate quartz nodules (qz).

Most of our current understanding of the deformation of porous limestones, as briefly summarized above, is based on experimental results obtained on dry materials. However, under typical upper crustal conditions, rocks are generally saturated with some aqueous pore fluid. Such pore water is expected to promote several time-dependent mechanisms which could affect the failure mode of the rock. First, in a partially undrained system, the presence of pore fluid can promote dilatancy hardening by temporarily reducing the effective pressure applied to the material. In that case, time dependency arises from the hydraulic diffusion process within the rock [*Rutter*, 1972; *Duda and Renner*, 2013]. Second, water can locally dissolve calcite, hence promoting pressure solution creep [e.g., *Zhang and Spiers*, 2005; *Zhang et al.*, 2010; *Croizé et al.*, 2013]. Third, water can also promote subcritical crack growth in calcite grains, as demonstrated by recent experimental results [*Røyne et al.*, 2011]. These three processes are expected to produce time-dependent, or, equivalently, strain rate-dependent, variations in the conditions of the brittle-ductile transition (as described by *Gratier et al.* [1999]) and more generally can potentially promote time-dependent creep under typical upper crustal conditions.

It is now well established that a wide range of water-saturated rocks, such as sandstones, granites, and basalts, can undergo time-dependent deformation within the brittle regime due to subcritical crack growth (see *Brantut et al.* [2013], for a review). This phenomenon is called brittle creep. Because of the potential competition between subcritical crack growth and other time-dependent mechanisms such as plastic flow or pressure solution [*Croizé et al.*, 2013], it is currently unclear whether the features of brittle creep will be the same in limestones as in other crustal rocks or even if brittle creep will occur at all in this material.

Aside from the early study of *Rutter* [1972] on low-porosity Solnhofen limestone and more recent data on high-porosity limestone [*Dautriat et al.*, 2011; *Cilona et al.*, 2012], experimental rock deformation data on natural porous limestones under water-saturated conditions are remarkably sparse. Most of the existing experimental work on carbonates has been performed on unconsolidated aggregates (see *Gratier et al.* [2013], for a review), either of pure calcite [e.g., *Zhang and Spiers*, 2005; *Zhang et al.*, 2010] or powdered limestones [e.g., *Baker et al.*, 1980; *Hellman et al.*, 2002; *Croizé et al.*, 2010]. Hence, our understanding of the coupling between microcracking, intracrystalline plasticity, and water-induced mechanisms such as pressure solution and subcritical cracking is insufficient for adequate prediction of the mechanical behavior of porous limestones under upper crustal conditions.

In the present study we investigated experimentally the mechanics of time-dependent creep in a porous, permeable, water-saturated limestone. We show experimental results from a series of triaxial deformation tests performed under both controlled stress (creep) and controlled strain rate conditions, within the brittle regime. We document the changes in porosity and wave velocities during deformation and use them as tools for quantifying the microstructural evolution of the samples. We subsequently describe the microstructures of deformed specimen and discuss the microscale deformation mechanisms that explain our observations. We finally discuss the implications of our results for deformation in the crust.

2. Experimental Methods

2.1. Starting Material and Sample Preparation

For this study, we selected a porous limestone from the South Coast of England, known as Pond freestone Purbeck limestone. Its mineralogical composition, obtained by X-ray diffraction analysis on bulk-powdered samples, is 80% calcite and 20% quartz. Figure 1 shows a micrograph of a thin section of the rock. It comprises peloids of size ranging from ≈100 μm up to ≈500 μm, composed of microcrystals of calcite,

Table 1. Summary of the Samples Tested and Experimental Conditions[a]

Sample	Laboratory	P_{eff} (MPa)	Strain Rate (s^{-1})	Peak Differential Stress (MPa)	Creep Differential Stress (MPa)	Minimum Strain Rate (s^{-1})	Final Strain (%)	Notes
pl16d	Strasb.	0	10^{-5}	75	–	–	–	dry, uniaxial
pl12w	Strasb.	10	10^{-5}	100	–	–	–	
PL-02	UCL	10	10^{-5}	76	–	–	0.8	V_p
PL-06	UCL	10	–	–	78 to 90	4×10^{-9}	1.0	V_p, 6 stress steps
PL-07	UCL	10	–	–	82 to 88	3×10^{-8}	1.0	V_p, 6 stress steps
PL-08	UCL	10	10^{-6}	83	–	–	0.8	V_p
PL-10	UCL	10	–	–	76	3×10^{-8}	0.9	V_p
PL-11	UCL	10	–	–	65 to 73	2×10^{-8}	0.9	V_p, one stress step
PL-13	UCL	10	–	–	80 to 85	1×10^{-9}	1.1	V_p, one stress step
PL-15	UCL	10	–	–	79	4×10^{-7}	0.8	V_p
pl13w	Strasb.	20	10^{-5}	107	–	–	–	
pl20w	Strasb.	20	10^{-5}	114	–	–	–	
PL-05	UCL	20	–	–	100	8×10^{-7}	1.5	V_p
PL-14	UCL	20	10^{-5}, 10^{-7}	–	–	–	–	V_p, strain rate steps
PL-16	UCL	20	10^{-5}, 10^{-7}	–	–	–	–	V_p, strain rate steps
PL-17	UCL	20	–	–	102	1×10^{-9}	–	V_p, stopped before failure
PL-19	UCL	20	–	–	104	4×10^{-10}	–	V_p, stopped before failure
PL-20	UCL	20	–	–	112	1×10^{-6}	1.4	V_p
PL-21	UCL	20	–	–	115	2×10^{-6}	1.3	V_p
PL-23	UCL	20	10^{-5}	122	–	–	1.5	V_p
pl09w	Strasb.	20	–	–	104	2×10^{-6}	1.4	
pl10w	Strasb.	20	–	–	99	5×10^{-8}	2.8	
pl14w	Strasb.	20	–	–	101	3×10^{-8}	4.1	
pl18w	Strasb.	30	10^{-5}	126	–	–	–	
pl03w	Strasb.	50	10^{-5}	duct.	–	–	–	
pl06w	Strasb.	60	10^{-5}	duct.	–	–	–	
pl11w	Strasb.	80	10^{-5}	duct.	–	–	–	
pl08w	Strasb.	–	–	–	–	–	–	hydrostat.

[a]For experiments performed under constant strain rate conditions, we report both the imposed strain rate and the observed peak differential stress. For experiments performed under creep conditions, we report the imposed differential stress and the minimum strain rate measured during the test. V_p denotes experiments during which *P* wave speeds were measured throughout deformation.

surrounded by a cement formed of large (typically > 100 μm) sparry calcite crystals. Quartz occurs as polycrystalline nodules distributed throughout the rock. The porosity of each sample was measured using the triple weight method and averaged 13.8%. The pore space is distributed into microporosity within the peloids and macroporosity occurring between the cement and the peloids. The dry uniaxial compressive strength of the rock was found to be 75 MPa. The permeability was measured at an effective pressure of 20 MPa using the constant flow rate method and is of the order of 10^{-16} m^2. This value is relatively high compared with that typical of low-porosity micritic limestones (such as Solnhofen limestone), the permeability of which is generally of the order of 10^{-19} m^2 or less [e.g., *Fischer and Paterson*, 1992]. This permeability of 10^{-16} m^2 ensured that the rock remained in a fully drained state throughout all our deformation experiments conducted at strain rates up to 10^{-5} s^{-1} and thus avoided any dilatancy hardening. The *P* wave speed

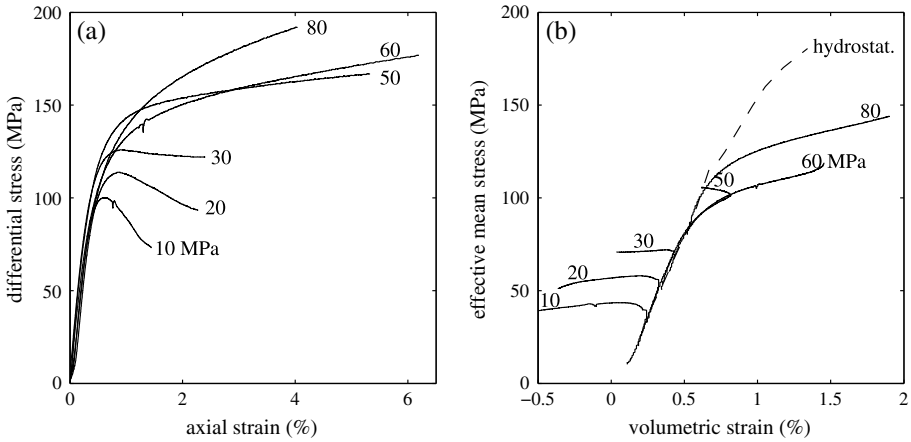

Figure 2. (a) Differential stress as a function of axial strain and (b) effective mean stress as a function of volumetric strain for samples of Purbeck limestone deformed at constant strain rate (10^{-5} s^{-1}). Figures on the curves denote the imposed effective pressure.

of the samples, measured under the test conditions (water saturated, at an effective pressure of 20 MPa), is 4.5 ± 0.1 km s^{-1}.

Cylindrical samples were cored, and the ends of the cylinders were ground to ensure a good parallelism (±10 μm). The samples were then saturated with distilled water for around 24 h prior to deformation. Note that the saturation period is not long enough to fully equilibrate the chemical composition of the pore water with that of the rock [e.g., *Zhang and Spiers*, 2005]; the pore fluid is thus initially undersaturated with respect to calcite.

2.2. Triaxial Deformation Apparatus

Triaxial deformation tests were performed using apparatus at the Experimental Geophysics Laboratory of the University of Strasbourg (see description in *Baud et al.* [2009]) and at the Rock and Ice Physics Laboratory of University College London (see description in *Heap et al.* [2009]). Both apparatus can apply independent, servo controlled, confining pressure, differential stress, and pore fluid pressure. The confining medium is oil. The axial shortening of the samples is measured outside the pressure vessel with a set of linear voltage differential transducers (LVDTs) recording the motion of the axial piston relative to the static frame of the pressure vessel. Axial shortening measurements are systematically corrected for the elastic deformation of the piston and sample assembly. Pore fluid volume is measured by tracking (with LVDTs) the position of the actuator of the servo controlled pore fluid intensifiers. Porosity change is calculated as the ratio of pore volume change over the initial sample volume. Strain is calculated as the ratio of the corrected axial shortening over the initial sample length, and strain rate is calculated as the time derivative of that strain.

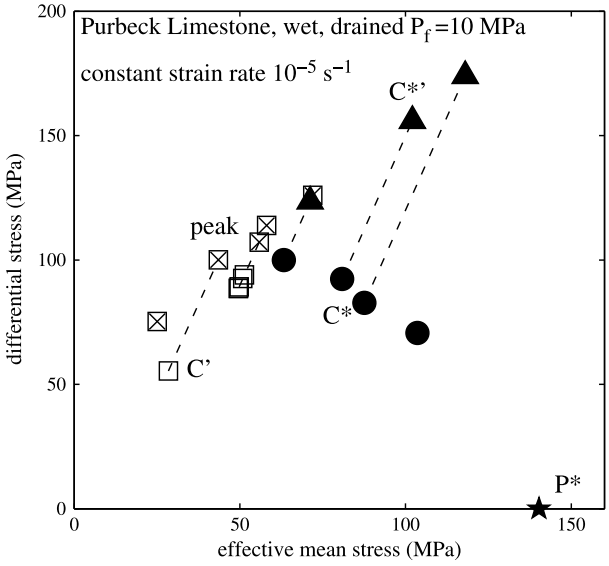

Figure 3. Peak stress (crossed squares) and thresholds C′ (empty squares), C* (filled circles), C*′ (triangles), and P* (star), shown in the stress space.

Samples were inserted into rubber jackets, positioned in the pressure vessel, and held at constant confining and pore pressure for 24 h prior to deformation. The experimental conditions for all tests are shown in Table 1. All tests were performed under drained conditions, at a constant pore fluid pressure

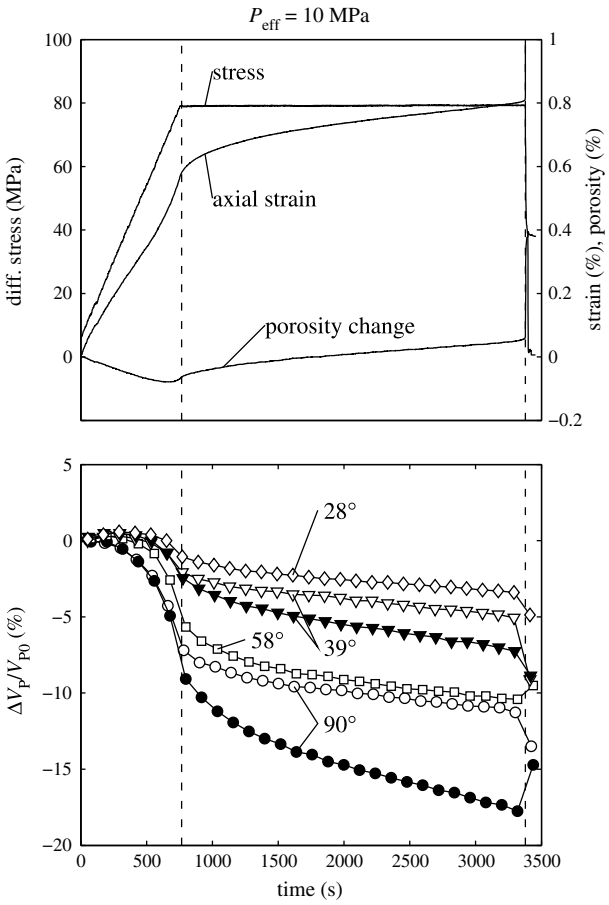

Figure 4. (top) Stress, strain, and pore volume change and (bottom) relative *P* wave speed variations during a conventional brittle creep test run at P_{eff} = 10 MPa. The imposed creep differential stress is Q = 79 MPa. The angles reported in degrees correspond to propagation path orientations with respect to the axis of compression. The first vertical dashed line represents the start of creep, and the second marks the time of sample failure.

of 10 MPa. The samples were deformed using either (1) an imposed, constant deformation rate (hereinafter termed "constant strain rate" experiments) or (2) an imposed, constant differential stress (termed "creep" experiments). In the latter case, the samples were initially loaded at an imposed constant loading rate (axial strain rate around 10^{-5} s^{-1}) until the target differential stress was reached. The differential stress was then maintained constant and the sample allowed to deform over extended periods of time; we term such tests "conventional" creep tests. In some cases, we sequentially stepped the imposed stress (we term these tests "stress-stepping" creep tests; see methodology in *Heap et al.* [2009]) or the imposed strain rate during deformation (see Table 1).

2.3. Elastic Wave Velocity Measurements

The samples deformed in the triaxial deformation apparatus installed at University College London were equipped with an array of 10 piezoelectric transducers, connected to a 10 MHz digital oscilloscope and a high-voltage source. All the transducers can be used either as receivers (in passive mode) or sources (converting a high-voltage impulse into a mechanical vibration). At regular time intervals during deformation, each sensor was sequentially used as a source while output waveforms were recorded on the remaining sensors. Precise *P* wave arrival times were extracted from those waveforms by using the cross-correlation technique described in *Brantut et al.* [2011, 2014]. The sampling rate of the original waveforms is 10 MHz, which results in raw absolute errors of the order of 1% on the measured *P* wave velocity. The relative precision between successive measurements is dramatically improved by the cross-correlation technique; in addition, the waveforms were resampled at 50 MHz with cubic splines prior to processing, which results in a relative precision of the order of 0.2%.

Assuming straight raypaths, the sensor arrangement gives access to the *P* wave speed along four different angles with respect to the axis of compression: 90° (radial), 39°, 58°, and 28° [see *Brantut et al.*, 2014].

3. Mechanical Behavior Under Constant Strain Rate Conditions

We first present the results from a series of tests performed at constant strain rate (10^{-5} s^{-1}), over effective pressures ranging from P_{eff} = 10 to 80 MPa (as mentioned above, the pore pressure was maintained at 10 MPa). Figure 2a shows the differential stress (denoted Q) as a function of axial strain, and Figure 2b shows the effective mean stress (calculated as $Q/3 + P_{eff}$) as a function of volumetric strain for the tests performed at P_{eff} = 10, 20, 30, 50, 60, and 80 MPa.

In experiments performed at $P_{eff} \leq 30$ MPa, the differential stress reaches a peak, followed by significant strain softening. Concomitantly, dilatancy was observed. These features are typical of the brittle regime. The samples were examined after deformation, and all exhibited a macroscopic shear fault. By contrast, the samples deformed at $P_{eff} \geq 50$ MPa all underwent strain hardening, as well as shear enhanced compaction.

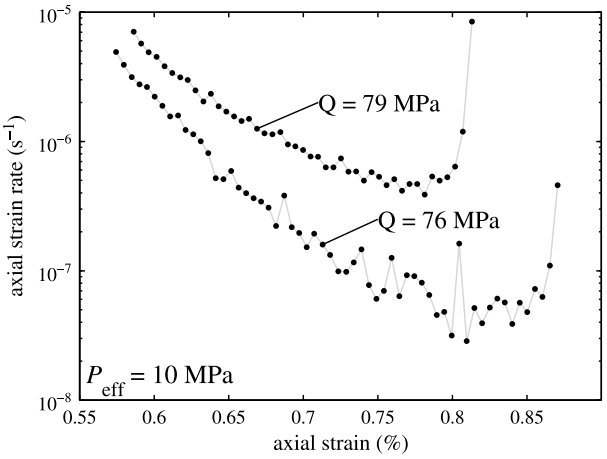

Figure 5. Axial strain rate as a function of axial strain for two different creep tests performed at P_{eff} = 10 MPa.

These samples showed no evidence of localized shear bands after deformation; instead, the deformation was distributed rather homogeneously throughout the material. These features are typical of the ductile regime. At P_{eff} = 50 and 60 MPa, the inelastic volumetric strain is initially compactant but becomes dilatant beyond 0.82 and 1.45% volumetric strain, respectively. The features observed in both the brittle and ductile regimes are consistent with previously reported results for dry porous limestones [*Baud et al.*, 2000; *Vajdova et al.*, 2004, 2012]. These constant strain rate tests were complemented by an experiment performed under purely hydrostatic conditions (dotted line in Figure 2); at $P_{eff} \approx$ 145 MPa, the compactant volumetric strain increases significantly with further increases in pressure, i.e., the material yields.

The thresholds for inelastic dilatancy (C′), inelastic compaction (C*), post yield dilatancy (C*′, marking the onset of net dilatancy after an episode of shear enhanced compaction), and hydrostatic yield pressure (P*) are represented in the stress space (differential stress versus effective mean stress) in Figure 3. At $P_{eff} \leq$ 20 MPa, the range of differential stress between the onset of dilatancy and the peak stress is of the order of a few tens of megapascals. At P_{eff} = 30 MPa, the rock is still macroscopically brittle but there is some inelastic compaction (C*) before the sample undergoes net dilatancy (C*′) at stresses very close (a few megapascals) to the peak stress. At this pressure, the behavior is in fact typical of the transition regime between brittle and ductile deformations. It has been shown by *Vajdova et al.* [2004] that this transition is more abrupt in limestone than in porous sandstone. Repeat experiments at the same pressure showed in particular significant differences in the post peak behavior and the occurrence in some cases of conjugate shear bands. In the remainder of the present study our focus is to examine the time-dependent behavior of Purbeck limestone in the brittle regime. Hence, we conducted these experiments at effective pressures in the range 10 to 20 MPa.

4. Mechanical Behavior Under Constant Stress Conditions

The time-dependent brittle behavior of Purbeck limestone was studied by performing a series of creep experiments at P_{eff} = 10 and 20 MPa. Figure 4 shows the results of a conventional brittle creep test performed at P_{eff} = 10 MPa with an imposed differential stress of Q = 79 MPa (sample PL-15 in Table 1). After the creep stress is reached and maintained constant, the axial strain first decelerates (over a period of around 2200 s) and then slowly accelerates until a sudden failure occurs (at this point the strain rate becomes so high that the servo controlled actuator is unable to maintain a constant stress). Concomitantly, the porosity change follows the same trend: dilatancy first decelerates and then accelerates until sample failure occurs. This behavior is typical of brittle creep, as reported in many other rock types such as sandstones and granites (reviewed in *Brantut et al.* [2013]).

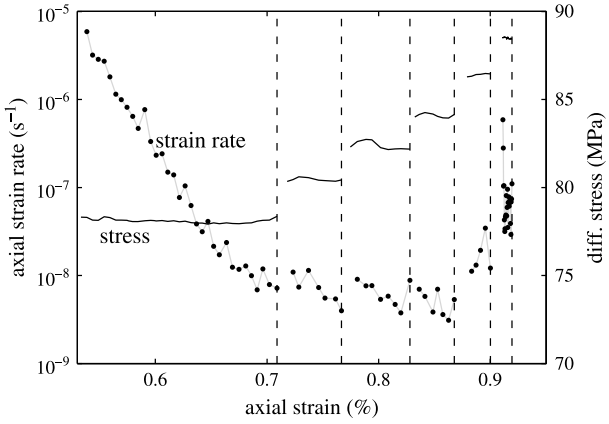

Figure 6. Axial strain rate as a function of axial strain for a stress-stepping creep tests performed at P_{eff} = 10 MPa.

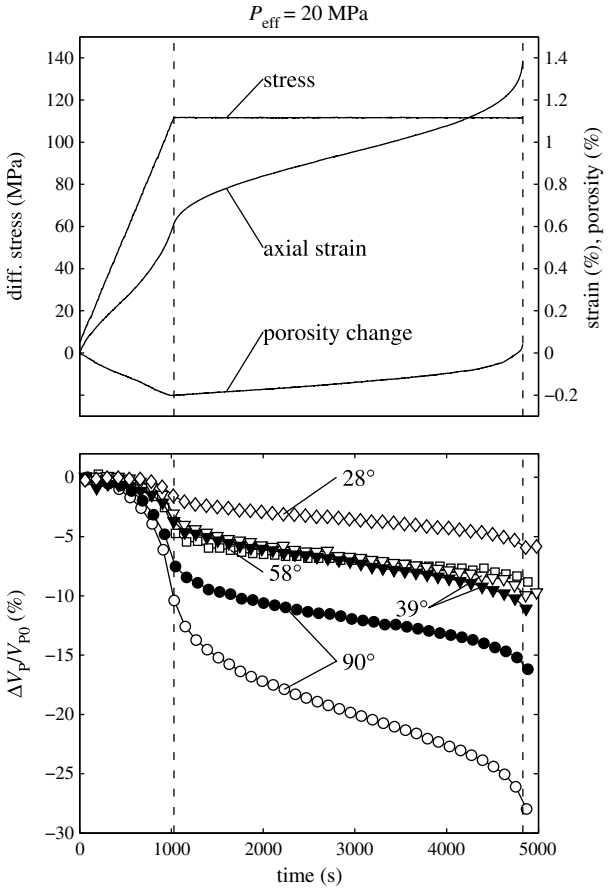

Figure 7. (top) Stress, axial strain, and porosity change and (bottom) relative *P* wave speed variations during a conventional brittle creep test run at P_{eff} = 20 MPa. The imposed creep differential stress is $Q = 112$ MPa. The angles reported in degrees correspond to propagation path orientations with respect to the axis of compression.

During deformation, the relative evolution of *P* wave speed depends on the propagation angle with respect to the compression axis. During the initial loading stage at constant loading rate, the sample first behaves elastically (before C′ is reached); the radial *P* wave speed (perpendicular to the compression axis) decreases slightly, while it increases slightly along subaxial propagation paths (at angles of 58°, 39° and 28° with respect to the compression axis), indicating the development of a stress-induced anisotropy. Then, beyond the onset of dilatancy, the *P* wave speed decreases along all orientations, with steeper decreases for radial than for subaxial orientations, indicating increased anisotropy. During creep, the change in *P* wave speed follows the same trend as that of the measured axial strain and porosity change: the decrease initially decelerates and is followed by rapid changes when the sample fails (the jumps at the last points in Figure 4 are artifacts due to the final measurement interval spanning the failure time). A significant divergence is observed between *P* wave speeds measured along the same orientation with respect to the compression axis but at different locations (see the two horizontal paths shown as filled and open circles and the two diagonal paths shown as filled and open triangles in Figure 4). This divergence indicates that heterogeneities in elastic properties are generated during deformation, in addition to the overall stress-induced anisotropy.

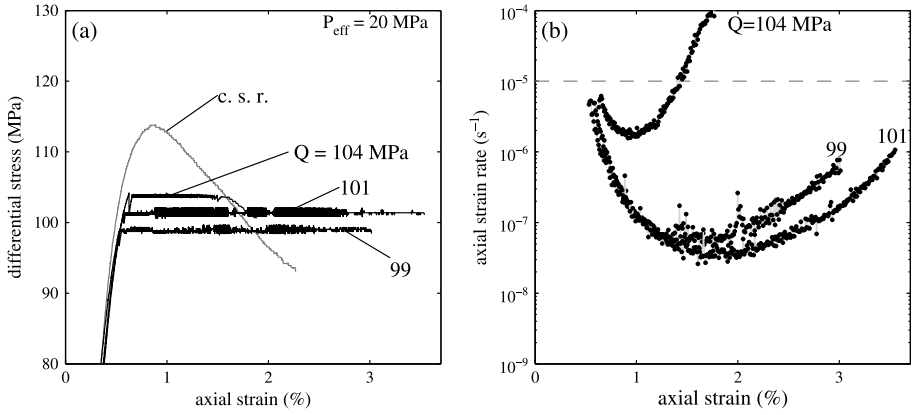

Figure 8. (a) Stress-strain curves for a constant strain rate test (at 10^{-5} s^{-1}, denoted "c. s. r.") and three conventional creep tests performed at P_{eff} = 20 MPa and (b) axial strain rate as a function of axial strain during the creep stages. The differential stress axis in Figure 8a is truncated to clarify the differences between the creep curves.

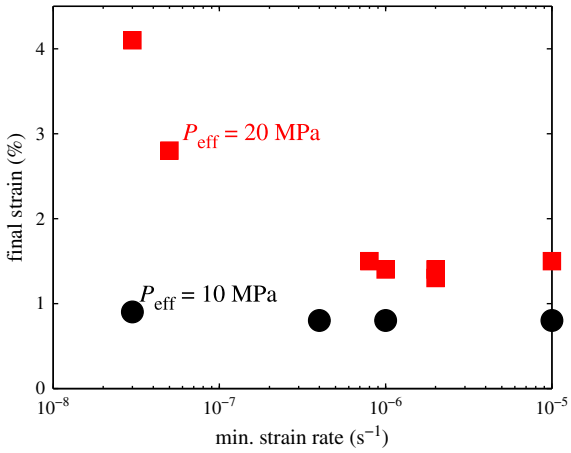

Figure 9. Final strain as a function of the minimum strain rate achieved during the deformation experiments. The data points at 10^{-5} s^{-1} correspond to constant strain rate tests, whereas all the other points correspond to conventional creep tests.

The evolution of strain rate as a function of strain is shown in Figure 5 for two conventional creep tests performed at $P_{eff} = 10$ MPa. We note that the creep strain rate is never constant: rather, it decreases gradually to a minimum and then increases up to failure.

In addition to these conventional creep tests, we also performed stress-stepping tests at $P_{eff} = 10$ MPa, in which the imposed creep stress is increased stepwise during deformation (see methodology in *Heap et al.* [2009]). Figure 6 shows the strain rate evolution as a function of axial strain during such a test. During the first creep stage (following the initial loading stage), the creep strain rate decreases substantially with increasing strain, down to 10^{-8} s^{-1} at 0.7% strain. In the following three steps, each time the differential stress is stepped up by a few MPa, an initial small jump in the strain rate ensues, followed by a gradual decrease. By contrast, following each of the last two stress steps (beyond 0.86% axial strain), the strain rate increases dramatically. We note that in all the tests performed at $P_{eff} = 10$ MPa (constant strain rate tests, as well as conventional and stress-stepping creep tests), the axial strain at failure was always in the narrow range from 0.8 to 1.1% (see Table 1).

The overall mechanical behavior during creep at $P_{eff} = 20$ MPa is quite similar to that at $P_{eff} = 10$ MPa. For example, Figure 7 shows the stress, axial strain, porosity change, and *P* wave speed evolution for a conventional creep test performed at $P_{eff} = 20$ MPa and $Q = 112$ MPa (sample PL-20 in Table 1). During creep, the axial strain again first decelerates and then accelerates up to failure. The trend is somewhat similar for the dilatant porosity change, although the decelerating phase is not as clearly visible as for the experiment at $P_{eff} = 10$ MPa (Figure 4). The relative evolution of *P* wave speeds is also qualitatively similar: a stress-induced anisotropy develops early on during initial loading and is amplified during creep. Again, we observe heterogeneity-induced divergence between the radial *P* wave speeds measured along different paths.

Several conventional creep tests were performed over a range of differential stresses at $P_{eff} = 20$ MPa. Figure 8a shows the stress-strain curves for three of those creep tests performed at $Q = 99$, 101, and 104 MPa, as well as for a constant strain rate test. The sample deformed at the highest creep stress undergoes accelerated deformation and failure when the axial strain reaches 1.6%, around the point where the creep stress crosses the decreasing stress sustained during the strain-softening phase of the constant strain rate test. By contrast, the behavior is qualitatively different for the two other experiments performed at lower differential stresses. Both samples were able to sustain much larger axial deformation without failure occurring. Figure 8b shows the evolution of strain rate as a function of axial strain during creep. For all three experiments, the creep strain rate first decreases, reaches a minimum, and then gradually increases with increasing deformation. During the test performed at the highest stress ($Q = 104$ MPa), the minimum creep strain rate is around 2×10^{-6} s^{-1} and is achieved at around 0.9% strain, which is very close to the amount of strain at the peak stress recorded during the test at constant strain rate. In the tests performed at lower stresses, the minimum creep strain rates are several orders of magnitude lower (of the order of 10^{-8} s^{-1}) and are only achieved at significantly higher strains (between 1.7 and 1.9%). Beyond the minimum, the creep strain rates again gradually increase with further deformation, well past the points where the creep stresses cross the stress sustained under constant strain rate conditions. The experiments were stopped without any macroscopic failure when the creep strain rate increased to around 10^{-6} s^{-1}, and the axial strain was around 3% (about twice the failure strain in the sample deformed at $Q = 104$ MPa).

The major difference in mechanical behavior between samples deformed at $P_{eff} = 10$ MPa and $P_{eff} = 20$ MPa is that, in the latter case, significantly more total strain can be achieved when the strain rate is lower (i.e., for lower creep stresses). This observation is clarified in Figure 9, which shows the final strain as a function

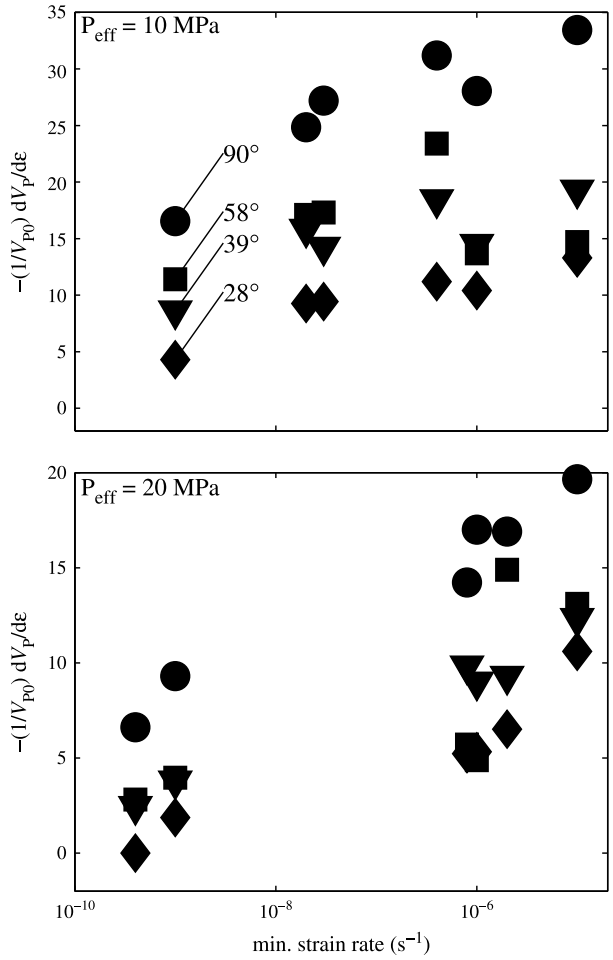

Figure 10. Average rate of relative decrease in *P* wave speed per unit axial strain as a function of the minimum strain rate achieved during the deformation tests (conventional creep and constant strain rate) performed at (top) $P_{eff} = 10$ MPa and (bottom) $P_{eff} = 20$ MPa. Circles correspond to radial paths (perpendicular to the compression axis), and squares, triangles, and diamonds correspond to path angles of 58°, 39°, and 28° with respect to the compression axis, respectively.

of the minimum strain rate achieved during the tests (conventional creep as well as constant strain rate) at $P_{eff} = 10$ MPa (black circles) and $P_{eff} = 20$ MPa (red squares).

The *P* wave speed evolution as a function of strain is qualitatively similar in all the tests, showing a continuous decrease with increasing axial deformation. The average rate of relative decrease in *P* wave speed per unit of axial strain, calculated as $(-1/V_{P0})dV_P/d\epsilon$, is reported in Figure 10 as a function of the minimum strain rate achieved during deformation. For each propagation angle, the *P* wave speed decreases more steeply with increasing strain (overall lower values of $(-1/V_{P0})dV_P/d\epsilon$) at $P_{eff} = 10$ MPa than at $P_{eff} = 20$ MPa. At 10 MPa effective pressure, the *P* wave speed decrease rate does not change significantly with decreasing minimum strain rate, except for the sample for which creep was slowest (of the order of 10^{-9} s^{-1}), which displays lower *P* wave speed decrease rates by about a factor of 2 compared to samples deformed at 10^{-5} s^{-1}. At $P_{eff} = 20$ MPa, the *P* wave speed decrease rate clearly diminishes with decreasing minimum strain rate. An end-member example of this trend is observed for the experiment in which the strain rate was lowest (4×10^{-10} s^{-1}): the *P* wave speed measured along the subaxial path at 28° from the compression axis remained approximately constant during creep, and hence, the *P* wave speed decrease rate was zero.

The effect of strain rate on the mechanical behavior and the evolution of *P* wave speed was also investigated by conducting strain rate-stepping deformation experiments. During these tests, samples were deformed under sequential constant strain rate conditions, during which the strain rate was stepped up and down at regular strain intervals. Figure 11 shows the results of such a test performed at $P_{eff} = 20$ MPa at stepped strain rates of 10^{-5} s^{-1} and 10^{-7} s^{-1}. The sample was first loaded at 10^{-5} s^{-1} until the porosity change showed net dilatancy (denoted D′, marked by a minimum in porosity; see *Heap et al.* [2009]). Immediately following this, the strain rate was stepped down by 2 orders of magnitude (marked by the first dashed line in Figure 11). During subsequent deformation at 10^{-7} s^{-1}, the stress relaxed by around 12 MPa, while the porosity evolution changed direction to reexhibit continued net compaction. When the strain rate was subsequently stepped back up to 10^{-5} s^{-1}, the signals reversed, with the stress increasing and the sample once again undergoing net dilatancy. In the subsequent steps down, stress relaxation was systematically observed immediately after the changes in strain rate and was followed by deformation at essentially constant stress, while the porosity kept increasing.

The overall evolution of *P* wave speed during the strain rate-stepping deformation experiments is qualitatively similar to that during the constant strain rate experiments: there is an overall decrease in *P* wave speed in all orientations during inelastic deformation, with larger decreases along radial orientations than along subaxial orientations (Figure 11). Heterogeneities in *P* wave speed also develop, as in the other tests

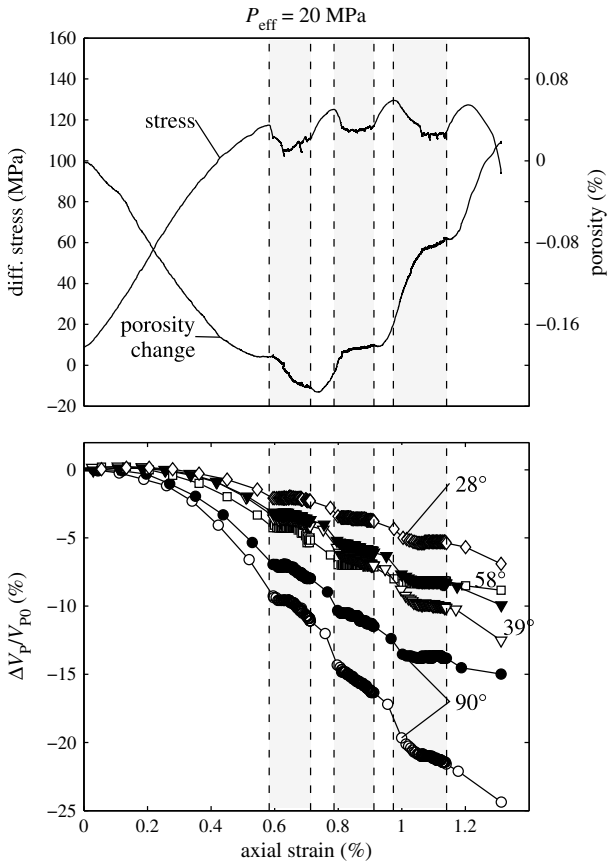

Figure 11. Mechanical behavior and *P* wave speed evolution with increasing strain during a strain rate-stepping test performed at P_{eff} = 20 MPa. The strain rate is 10^{-5} s^{-1} and was stepped down to 10^{-7} s^{-1} during the strain intervals marked by the dashed lines.

(e.g., Figures 4 and 7). The decrease in *P* wave speed during the deformation steps at 10^{-7} s^{-1} is less marked than during the deformation steps at 10^{-5} s^{-1}. Part of this effect can be attributed to the stress relaxation that accompanies the step changes in strain rate. However, during the last low strain rate step shown in Figure 11, the stress remains constant during most of the deformation (from 1.06% to 1.14%), while the *P* wave speeds in all subaxial orientations remain essentially constant. When the strain rate is stepped up again in the final stage, the decrease in *P* wave speed in all orientations resumes.

5. Microstructure

Polished thin sections were made from specimen pl13w, pl09w, and pl14w, deformed at P_{eff} = 20 MPa under both creep and constant strain rate conditions, and analyzed using both optical and scanning electron microscopy (SEM).

Figure 12 shows a representative set of the microstructures observed in the deformed samples. Optical observations under crossed polars (Figure 12a) show extensive twinning of the large calcite crystals that form the cement. These large calcite grains also contain thin through-going fractures. By contrast, the quartz grains remain mostly intact throughout the sample. SEM observations (Figures 12b–12d) confirm that the large calcite crystals within the cement are highly fractured by long and thin subaxial cracks, sometimes forming en échelon structures (Figure 12c). Several occurrences of wing cracks were also observed (Figure 12d). Within a given calcite crystal, most cracks follow a similar orientation, likely to be dictated by the combination of the imposed stress and the crystallographic weakness planes (cleavage) of the crystal.

Peloids are also fractured by subaxial cracks, the morphology of which is strongly different from the intragranular cracks within the cement (see Figures 12e and 12f). Intrapeloidal cracks are very tortuous and generally follow the boundaries of the micrometric crystals forming the peloids. Peloid rims generally comprise a higher-porosity aggregate compared with the centermost parts; in the rims, the large intrapeloid cracks become diffuse and tend to lose their continuity.

The long, thin intragranular cracks within the cement also generally terminate at the interface between the cement and the microporous rims of the peloids (see Figures 12b and 12c). Figure 13a provides an SEM image showing a detailed view of the termination of such an intragranular crack at the fine grained, porous rim of a peloid. The arrest is very sudden, and there is no visible indication of deformation within the porous aggregate. By contrast, as shown in Figure 13b, in some areas the intrapeloid cracks and the intragranular cracks in the cement are wide enough to cut across the porous rim of the peloids. Even in these relatively rare cases, the crack network within the porous rim is barely observable, and most of the local deformation seems to be distributed throughout the aggregate.

As a comparison, Figure 14 shows SEM images of sample pl14w, deformed under creep conditions up to a similar amount of strain (around 3%; see Table 1). Despite the differences in mechanical behavior observed

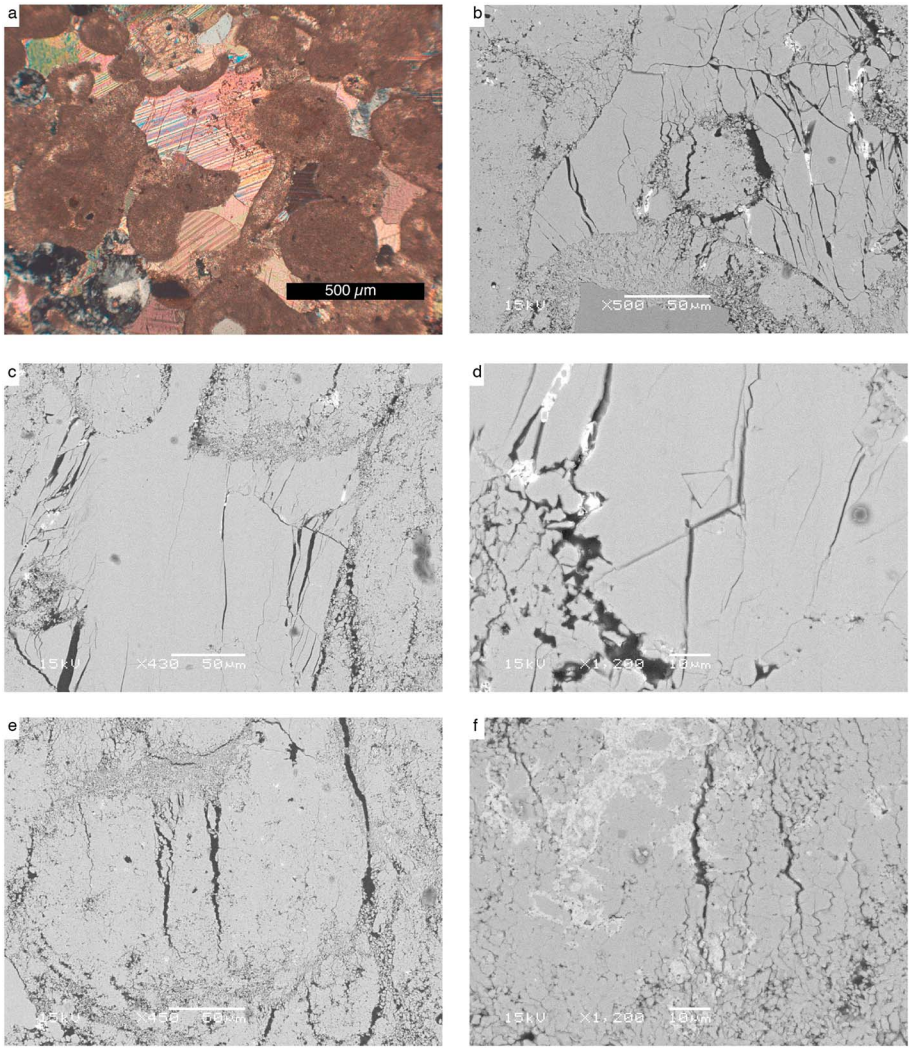

Figure 12. Microstructures in sample pl13w deformed at constant strain rate (10^{-5} s^{-1}) and P_{eff} = 20 MPa. The axis of compression is vertical in all images. (a) Micrograph under crossed polars, showing highly twinned and cracked calcite cement, and intact quartz grains (shades of grey). (b–d) Scanning electron microscope backscattered electron (SEM-BSE) images showing long thin cracks and en échelon wing cracks in the calcite cement. Most cracks in the cement do not cross cut the neighboring peloids but terminate at the interface. (e–f) SEM-BSE images showing tortuous cracks in the peloids. The cracks become diffuse at the outer edge of the peloids, where porosity is locally higher.

in Figure 8 between samples pl13w (constant strain rate) and pl14w (creep at 3 × 10^{-8} s^{-1} up to 4.1% strain), no obvious qualitative differences can be detected between the microstructures of these samples. The features observed after creep deformation in Figure 14 are essentially the same as those observed after constant strain rate deformation in Figures 12 and 13: long thin cracks are present in the calcite cement, whereas the peloids contain a network of tortuous microcracks.

6. Discussion

The overall mechanical behavior of our Purbeck limestone under water-saturated conditions is very similar to that reported for other porous limestones under dry conditions [e.g., *Vajdova et al.*, 2004]: the rock is brittle and dilatant at low effective pressures (here for $P_{eff} \leq$ 20 MPa) and becomes ductile and compactant at high effective pressures. Throughout deformation of the brittle regime, *P* wave speed measurements indicate the development of crack-induced anisotropy, together with heterogeneities most likely associated with progressive strain localization in the samples.

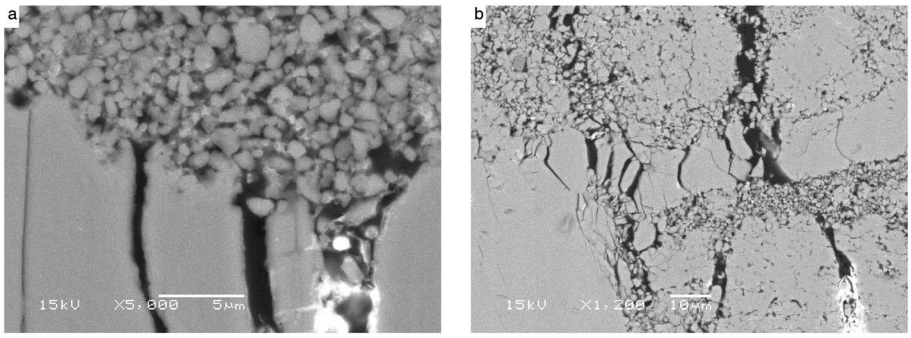

Figure 13. SEM-BSE images of sample pl13w deformed at constant strain rate (10^{-5} s^{-1} and P_{eff} = 20 MPa). The axis of compression is vertical. Close-up view of (a) cracks originating in the calcite cement and terminating at the interface with a peloid (appearing as the microporous aggregate at the top of the picture) and (b) cracks cross-cutting both the calcite cement and the peloids.

Microstructural observations of the samples deformed at P_{eff} = 20 MPa confirm that the major deformation process under this pressure condition is microcrack growth, which is consistent with the macroscopic mechanical behavior observed in experiments performed at constant strain rate. Because of the heterogeneous microstructure of the rock, two types of cracks coexist: in the calcite cement, thin, straight intragranular cracks are present, whereas in the peloids the cracks are mostly intergranular and tortuous (following grain boundaries).

6.1. Phenomenology of Brittle Creep

The results from our creep experiments show that the macroscopic phenomenon of brittle creep, as documented in other rock types such as sandstones, granites, or basalts [*Brantut et al.*, 2013], also occurs in this porous limestone. When the rock samples are deformed under constant stress conditions, the deformation follows a decelerating phase (commonly called primary creep), then an inflection point, and finally an accelerating phase (tertiary creep), typical of brittle creep with progressive microcrack damage [*Brantut et al.*, 2013].

At P_{eff} = 10 MPa, the features of brittle creep in Purbeck limestone are very similar to those in other porous rocks, such as in Darley Dale sandstone [*Baud and Meredith*, 1997; *Heap et al.*, 2009]. The total axial strain at failure and the rate of decrease in *P* wave speed are only weakly influenced by the loading and strain rate history (see Figure 9), which is consistent with similar observations from experiments performed on sandstones [*Baud and Meredith*, 1997; *Heap et al.*, 2009; *Brantut et al.*, 2014], granites [*Kranz and Scholz*, 1977], and basalts [*Heap et al.*, 2011]. In sandstones and igneous rocks, as well as in ceramics, it is generally accepted that brittle creep is driven by microscopic subcritical crack growth within grains and along grain boundaries

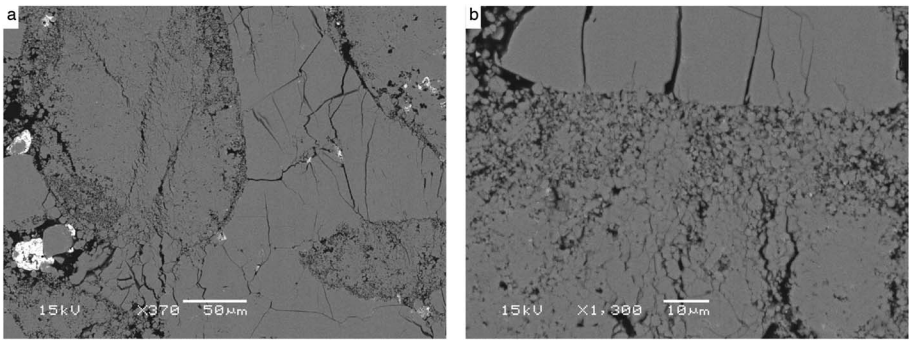

Figure 14. SEM-BSE images of sample pl14w deformed under creep conditions (minimum strain rate 3×10^{-8} s^{-1} and P_{eff} = 20 MPa). The axis of compression is vertical. (a) Long and thin cracks are observed in the calcite cement, (b) whereas a network of tortuous cracks is present in the micritic peloids. Figure 14a shows an example of microscale conjugate shear bands within a peloid.

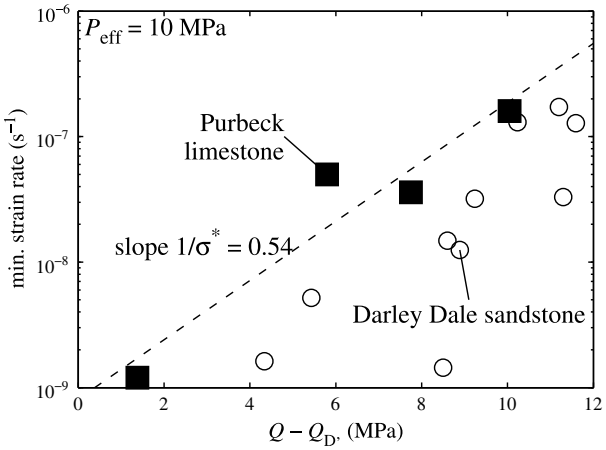

Figure 15. Minimum creep strain rate as a function of the applied differential stress (Q) offset by the differential stress at D′ ($Q_{D'}$), for conventional creep experiments performed at P_{eff} = 10 MPa. Data points for Darley Dale sandstone, from *Brantut et al.* [2013], are shown for comparison.

[see *Lawn*, 1993; *Brantut et al.*, 2013, and references therein]. The phenomenon of subcritical crack growth has also been observed experimentally in calcite in wet environments [e.g., *Røyne et al.*, 2011]. Hence, subcritical crack growth in calcite can explain the origin of time-dependent fracture in Purbeck limestone and the similarity between the features observed in this limestone at P_{eff} = 10 MPa and in other rock types.

Brittle creep is, in general, extremely sensitive to the applied stress, with changes in differential stress of the order of a few MPa inducing changes in strain rate of up to several orders of magnitude [e.g., *Brantut et al.*, 2013]. The stress sensitivity of brittle creep strain rate is commonly obtained by quantifying the minimum strain rate achieved during creep (usually termed "secondary creep strain rate") as a function of the imposed stress, for a series of conventional creep experiments. However, the theoretical basis for this approach is questionable, as the inflection point giving minimum strain rate generally represents a dynamically determined transition state rather than a steady state. Moreover, the comparison of brittle creep strain rates between experiments performed on different samples is often difficult, because the natural variability between samples tend to induce large variations in the creep strain rates [e.g., *Heap et al.*, 2009]. As shown by *Brantut et al.* [2013], this difficulty can be overcome by offsetting the stress scale by the differential stress reached when deformation becomes dominated by dilatancy (denoted D′ and defined as the minimum in the porosity change curve; see *Heap et al.* [2009]). The stress sensitivity of brittle creep in Purbeck limestone at P_{eff} = 10 MPa is illustrated in Figure 15, which is a plot of the minimum creep strain rate as a function of the imposed differential stress Q (offset by the stress at D′, denoted $Q_{D'}$). Data for Darley Dale sandstone under the same conditions are also shown for comparison. The minimum strain rate is broadly proportional to an exponential of the stress,

$$\min\{\dot{\epsilon}\} \propto \exp\left((Q - Q_{D'})/\sigma^*\right), \quad (1)$$

where σ^* is an activation stress, equal to 1.9 MPa in the fit of the limestone data shown in Figure 15. This stress dependency is within the same range as that determined for Darley Dale sandstone at the same effective pressure, for which σ^* ranges from 1.0 to 2.2 MPa [*Brantut et al.*, 2014]. Despite the strong differences in mineralogy and microstructure between these two rocks, this quantitative agreement is perhaps not surprising since (1) the initial porosity of Purbeck limestone is very similar to the porosity of Darley Dale sandstone and (2) the stress sensitivity of subcritical crack growth (or, more precisely, the sensitivity of crack growth rate on the energy release rate at the crack tip) in calcite is close to that of quartz [*Røyne et al.*, 2011; *Darot and Guéguen*, 1986].

The stress-stepping experiments performed at P_{eff} = 10 MPa (see Figure 6) indicate that the evolution of strain rate during creep is influenced not only by the imposed stress but also by the amount of accumulated strain. At low strains, the strain rate decreases with increasing strain, whereas past some critical strain, the strain rate increases with further deformation (Figure 6). A similar pattern is also observed in conventional (constant stress) creep tests (e.g., Figure 5), where we see that the accumulated strain exerts a strong control on the evolution of strain rate at a given constant stress level. This strain-driven evolution is qualitatively similar to that observed in porous sandstones by *Brantut et al.* [2014], who interpreted strain as an internal state variable in a rate- and state-dependent deformation law based on microscale stress corrosion cracking. Our observations on Purbeck limestone are too limited to develop such a detailed description of rate-dependent brittle deformation. However, the qualitative macroscopic similarities between the rate-dependent behavior of Purbeck limestone and the sandstones analyzed by *Brantut et al.* [2014], and the similar origin of the rate dependency in both these rock types (subcritical crack growth) strongly suggest

that the rate- and state-dependent brittle deformation law should also be applicable to porous limestones in the low effective pressure regime.

In the deformation experiments (both creep and constant strain rates) performed at $P_{eff} = 20$ MPa, the samples remain macroscopically brittle. The continuous decrease in *P* wave speed with increasing deformation, the occurrence of dilatancy, and the microstructural observations all indicate that the dominant microscale deformation process is crack growth. However, the behavior during creep deformation, or more generally, with decreasing strain rates, shows some unexpected characteristics.

First, the total strain accumulated prior to failure increases dramatically with decreasing strain rate (Figure 9). As also observed in Figure 8, this strain accumulation occurs mostly at strain rates well below the strain rate of 10^{-5} s^{-1}, which is taken as a reference for the short-term mechanical behavior. A surprising but robust observation is that the constant stress during creep can be maintained well above the stress sustained at constant strain rate (10^{-5} s^{-1}), without any sudden acceleration in deformation, depending on the stress level (see Figure 8a). This is in sharp contrast with the result at $Q = 104$ MPa and also with observations of brittle creep in other rock types, such as sandstones, where the strain rate accelerates dramatically as soon as the creep stress becomes equal to the stress sustained at constant strain rate [*Brantut et al.*, 2014]. Specifically, *Brantut et al.* [2014] have shown that the creep strain rate is proportional to an exponential of the difference between the imposed creep stress and the stress sustained at constant strain rate. However, this empirical law (observed in sandstones) is clearly not valid for the porous limestone studied here at $P_{eff} = 20$ MPa and $Q \leq 101$ MPa. The large additional deformation that can be accumulated at low strain rate suggests that an additional deformation mechanism (other than crack growth) is activated when deformation is slow enough.

Second, the decrease in *P* wave speed per unit strain decreases with decreasing strain rate (Figure 10). *P* wave speed is very sensitive to microcrack density [e.g., *Guéguen and Kachanov*, 2011]: the decrease in *P* wave speed per unit strain is thus a good proxy for the microcrack density evolution per unit strain [e.g., *Ayling et al.*, 1995]. The data shown in Figure 10 indicate that, for a given increment of axial strain, the corresponding increment in microcrack density tends to be smaller at lower strain rate. This observation is again in contrast with those for sandstones [*Brantut et al.*, 2014], which show that the rate of decrease in *P* wave speed (per unit strain) is not significantly dependent on the strain rate history. This difference in behavior between our porous limestone and the porous sandstones is consistent with the suggestion that the contribution of another deformation mechanism, specific to porous limestone and different from subcritical crack growth, becomes significant at low strain rates.

Third, the strain rate-stepping experiment indicates that the compactant versus dilatant behavior of the limestone depends on the imposed strain rate: when the strain rate is stepped down from 10^{-5} s^{-1} to 10^{-7} s^{-1}, comparatively more compaction is observed. This is clearly manifested by the switch from dilatancy-dominated to compaction-dominated deformation just after the first downstep, in Figure 11.

6.2. Deformation Mechanisms at Low Strain Rate

In order to explain our experimental observations at $P_{eff} = 20$ MPa, we therefore need to identify an inelastic deformation mechanism that (1) is active in limestone under the deformation conditions of our experiments (room temperature, P_{eff} of the order of 20 MPa), (2) is compactant, and (3) allows the accommodation large strains when strain rate decreases below $\approx 10^{-7}$ s^{-1}.

Calcite has several crystal plasticity mechanisms active at room temperature over a range of critically resolved shear stresses k_c [*Turner et al.*, 1954; *de Bresser and Spiers*, 1993]: *e*-twinning ($k_c \approx 6$ MPa), *r*-glide ($k_c \approx 144$ MPa), and *f*-glide ($k_c \approx 218$ MPa). Twins are ubiquitously observed in the calcite cement of the deformed samples (Figure 12), whereas they are scarce in the intact material. However, twinning in calcite is essentially stress and grain size dependent rather than strain rate dependent [e.g., *Rowe and Rutter*, 1990], and it is not clear how it could contribute to significant compaction. The critically resolved shear stresses needed to activate *r*- and *f*-glide are higher than the applied stresses in all our experiments conducted at $P_{eff} = 20$ MPa; thus, it is unlikely that these intracrystalline slip systems are the sole origin of the observed time-dependent effects. However, intracrystalline plastic deformation may be expected to occur at the microcrack tips (if not in the bulk) and hence may affect how microcracks propagate and interact. If more efficient plastic flow is allowed at crack tips due to lower crack growth rates, we would expect crack blunting,

Table 2. Parameter Values Used to Construct the Deformation Mechanism Map

Parameter	Value
Diffusivity[a], D	1×10^{-10} m^2 s^{-1}
Solubility of calcite[b], C	2.19×10^{-6} m^3 m^{-3}
Aqueous film thickness[c], S	1 nm
Precipitation rate[d], k_p	1.61×10^{-13} m s^{-1}
Molar volume of calcite, Ω,	3.69×10^{-5} m^3 mol^{-1}
Activation stress, σ^*,	1.85 MPa
Short-term peak stress[e], Q_{peak}	90 and 120 MPa

[a]From *Nakashima* [1995].
[b]From *Plummer and Busenberg* [1982].
[c]From *Renard et al.* [1997].
[d]From *Inskeep and Bloom* [1985]; value divided by 100 to simulate the presence of impurities.
[e]Representative values obtained from tests at constant strain rate at $P_{eff} = 10$ and 20 MPa, respectively.

overall less efficient crack propagation (shorter cracks), and less crack interaction due to plastic shielding [*Lawn*, 1993]. From a qualitative point of view, these effects can clearly contribute to the change in behavior observed at low strain rates at $P_{eff} = 20$ MPa. Indeed, shorter cracks and fewer crack interactions are expected to produce higher overall strain at failure (since more cracks can be accommodated before they interact and coalesce) and a less dramatic decrease in P wave speed (since crack density is proportional to the cube of crack length). However, the microstructural complexities of Purbeck limestone, together with the intrinsic complexity of the couplings between crack growth and microplasticity, make macroscopic quantitative predictions extremely difficult.

Another possible candidate for our extra deformation mechanism is pressure solution in calcite (see *Gratier et al.* [2013], for a review). At room temperature, the solubility of calcite is high (compared with quartz or feldspar, which are the major constituents of sandstones), and Purbeck limestone contains fine grained, high-porosity calcite aggregates in the form of peloids. In addition, pressure solution is fundamentally a compactant mechanism, when pores are present, and therefore consistent with our observations. Our microstructural observations do not show any direct evidence of pressure solution seams at grain contacts, even within the microporous rims of the peloids. However, any direct evidence would likely be barely observable considering the small strains involved and masked by the overwhelming presence of cracks. The detection of *newly created* pressure solution features is also rendered difficult, if not impossible, by the very small grain size (of the order of a few microns or less) within the peloids and the potential preexisting pressure solution seams which were formed during the diagenesis of the rock. Hence, the absence of direct microstructural evidence of pressure solution does not by itself invalidate the possibility that pressure solution could contribute significantly to deformation at low strain rates.

Zhang and Spiers [2005] and *Zhang et al.* [2010] have shown that, at room temperature, wet granular calcite undergoes diffusion-limited pressure solution creep at strain rates in the range 10^{-9} s^{-1} to 10^{-4} s^{-1} and can be responsible for several percent of shortening strain, depending on the imposed stress, porosity, and fluid pressure. Accurate predictions of creep strain rates associated with pressure solution at grain contacts are, in general, not available, since pressure solution is strongly influenced by the local grain contact geometry, impurities in the fluid and solid phases, and local stresses [e.g., *Lehner*, 1990]. However, we can use the thermodynamics-based creep laws provided by *Zhang et al.* [2010] in order to obtain an order of magnitude estimate of the strain rate associated with pressure solution. The phenomenon of pressure solution creep requires dissolution of the solid at grain contacts, diffusion of the solute along the grain boundaries, and precipitation in the pore space, the creep strain rate being dictated by the slowest of these processes. Under ambient temperature and water-saturated conditions, dissolution of calcite is, in general, fast enough so that dissolution-limited pressure solution creep is rarely observed. Hence, we restrict our analysis to diffusion- and precipitation-limited pressure solution creep. The rate equation for diffusion-limited creep given by *Zhang et al.* [2010] is of the form

$$\dot{\epsilon}_d = DCS(1/d^3)\left[\exp\left(\frac{B\sigma_e\Omega}{RT}\right) - 1\right] f_d, \tag{2}$$

where D is the diffusivity of ions within the grain boundary fluid, C is the solubility of calcite in water, S is the mean width of the fluid layer at grain boundaries, d is the mean grain diameter, σ_e is the effective axial stress (equal to $Q + P_{eff}$), B is a stress amplification factor at grain contacts, Ω is the molar volume of calcite, R is the gas constant, T is the absolute temperature, and f_d is a nondimensional function of the grain-packing geometry. For precipitation-limited creep, the rate equation reads [*Zhang et al.*, 2010]

$$\dot{\epsilon}_p = (k_p/d)\left[\exp\left(\frac{B\sigma_e\Omega}{RT}\right) - 1\right] f_p, \tag{3}$$

where k_p is the precipitation rate and f_p is a nondimensional factor depending on the grain-packing geometry. The precipitation rate constant k_p for calcite can significantly vary depending on the presence of impurities. In the precipitation-limited pressure solution creep regime, *Zhang et al.* [2010] showed that impurities in the form of magnesium ions can decrease precipitation rates by as much as 2 orders of magnitudes. In order to account for such impurities in our natural limestone, we choose a value of $k_p = 1.61 \times 10^{-11}$ m s^{-1}, which is 2 orders of magnitude lower than that measured in pure calcite at 25°C [*Inskeep and Bloom*, 1985]. When the grain packing is regular, the factors B, f_d, and f_p can be calculated explicitly. However, the irregular nature of the microstructure of our natural limestone makes such detailed calculations futile. Here, in the spirit of making order of magnitude estimates, we will assume that B is of the order of 1 (we neglect stress amplification at grain contacts) and estimate $f_d \approx 240$ and $f_p \approx 20$ from a simplified packing model with ≈20% porosity [*Zhang et al.*, 2010]. Other parameter values, taken from the literature, are reported in Table 2.

In order to compare the pressure solution creep strain rate to the brittle creep strain rate (originating from subcritical crack growth in calcite), we need to estimate the latter by a macroscopic rheological law. Again, it is theoretically possible to obtain such a law from first principles, by making precise assumptions about the microcrack network geometry, subcritical crack growth rates, and upscaling techniques [e.g., *Brantut et al.*, 2012]. However, such procedures rely on a number of independent micromechanical parameters which are not accessible for our limited data set. Alternatively, we can base our macroscopic brittle creep rheological law on the semiempirical approach outlined by *Brantut et al.* [2014], in which the brittle creep strain rate is expressed as

$$\dot{\epsilon} = \dot{\epsilon}_0 \exp\left((Q - Q_0)/\sigma^*\right), \tag{4}$$

where $\dot{\epsilon}_0$ is a reference (constant) strain rate, Q_0 is the differential stress sustained by the rock at the reference strain rate, Q is the applied differential stress, and σ^* is an activation stress. This macroscopic law is valid *throughout* all phases of creep deformation[*Brantut et al.*, 2014]: it captures the evolution of creep strain rate with increasing deformation, since the sustainable stress Q_0 evolves with deformation. The physical validity of (4) hinges upon the requirement that the stress difference $Q - Q_0$ must be taken at a fixed microstructural state of the samples [*Brantut et al.*, 2014]. A consequence of equation (4) is that the minimum strain rate achieved during creep is

$$\min\{\dot{\epsilon}\} = \dot{\epsilon}_0 \exp\left((Q - Q_{\text{peak}})/\sigma^*\right), \tag{5}$$

where Q_{peak} is the peak stress measured at constant strain rate $\dot{\epsilon}_0$. Equation (5) is of the same form as equation (1), and the activation stress σ^* is therefore expected to be the same as the one estimated from Figure 15. This is justified because (1) the stress at D′ (which we recall is a reference turning point where the deformation becomes dominated by dilatancy) is a measure of the strength of the material at a point during deformation where the microstructural state of all the tested samples is comparable (which validates the use of equation (4)), (2) σ^* does not depend upon the effective confining pressure [*Brantut et al.*, 2014], and (3) for a given effective confining pressure, the difference between $Q_{D'}$ and Q_{peak} is generally constant [*Brantut et al.*, 2013]. This last point was validated for Purbeck limestone using our data at $P_{\text{eff}} = 10$ MPa. The minimum strain rate during brittle creep can then be computed by using $\dot{\epsilon}_0 = 10^{-5}$ s^{-1} and representative values of Q_{peak} measured at this constant strain rate (reported in Table 2).

Using equations (2), (3), and (5) together with the parameter values reported in Table 2, we can construct a deformation mechanism map. Here, for simplicity, we assume that the strain rates for the two mechanisms can be superimposed, i.e., we neglect any potential coupling between crack growth and pressure solution rates. Such coupling will be discussed later. Figure 16 shows contour maps of *minimum* strain rate as a function of differential stress and average grain size for $P_{\text{eff}} = 10$ MPa (left) and $P_{\text{eff}} = 20$ MPa (right). These two diagrams are qualitatively similar; the strong quantitative difference is that the stress scale is shifted toward high values at higher P_{eff}. A feature well illustrated by the maps is that the stress sensitivity of the deformation rate is much smaller in the pressure solution-dominated regime (for which it is given by the factor $RT/(B\Omega)$) than in the subcritical crack growth-dominated regime (in which it is given by σ^*). The grain size observed within the porous rims of the peloids is of the order of 1 μm. The deformation mechanism map shows that, in these rim zones, the pressure solution creep rate is expected to be much faster than the stress corrosion creep rate. By contrast, the grain size of the calcite cement is much larger; of the order of 50 to

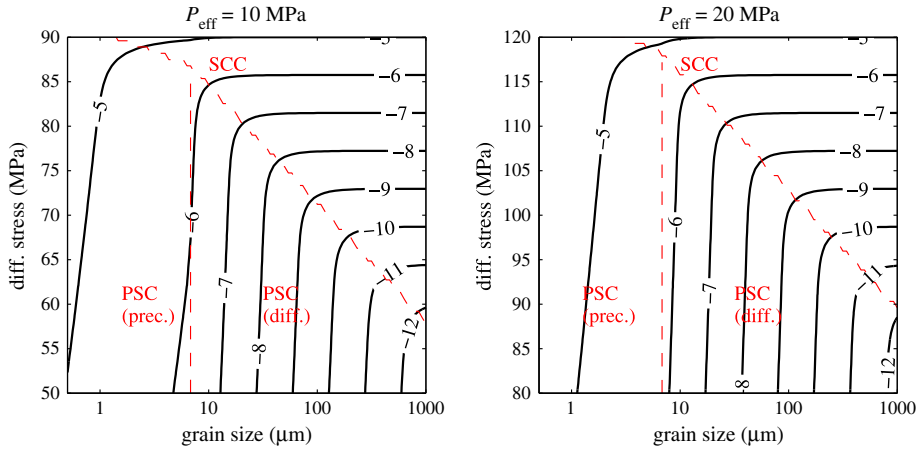

Figure 16. Deformation mechanism maps for Purbeck limestone at (left) $P_{eff} = 10$ MPa and (right) $P_{eff} = 20$ MPa. Only two mechanisms are considered: stress corrosion creep (SCC), modeled using equation (5), and pressure solution creep (PSC), modeled with equation (2) (diffusion limited, "diff.") and (3) (precipitation limited, "prec."). Strain rate from the two mechanisms are assumed to be additive. The dashed red line marks the boundaries of domains in which each mechanism is dominant.

100 μm. Hence, stress corrosion crack growth is likely to be the dominant deformation mechanism in the cement in the high-stress regime. According to the deformation mechanism maps, for a grain size of 100 μm (which would be appropriate for the cement), the switch in mechanism from stress corrosion creep to pressure solution creep (limited by diffusion for this grain size) would occur at a strain rate of slightly less than 10^{-9} s^{-1} and a differential stress of around 70 MPa at $P_{eff} = 10$ MPa and between 10^{-8} and 10^{-9} s^{-1} and a differential stress of around 100 MPa at $P_{eff} = 20$ MPa. These threshold strain rates for the switch in dominant deformation mechanism are consistent with our experimental observations (Figures 9 and 10). Note that the stress sensitivity of pressure solution creep would increase with increasing B, which typically ranges from 1 to 3; the corresponding characteristic stress (given by $RT/(B\Omega)$) ranges from 67.6 to 22.5 MPa, respectively. Choosing, say, $B = 3$ would push the transition in mechanism to higher strain rates by around 1 order of magnitude.

Coupling between crack growth and pressure solution also introduces more complexity in the determination of the dominant deformation mechanism. As shown by *Gratier* [2011], fracturing generally increases pressure solution rates by locally reducing grain size and facilitating fluid diffusion. Brittle deformation tends to become more cataclastic and distributed as the brittle-ductile transition is approached [e.g., *Wong and Baud*, 2012], and hence, the coupling between microcracking and pressure solution is expected to become stronger near this transition. Consequently, deformation at $P_{eff} = 20$ MPa is more prone to inducing enhanced pressure solution creep compared with deformation at lower effective pressures; which is again consistent with our observations. Quantitative predictions of the coupled effects of crack growth and pressure solution on macroscopic deformation rates are currently unavailable. In absence of better coupled models, the simple deformation mechanism map shown in Figure 16 should therefore be considered as a first-order guide: It is likely that the difference in strain rate at the transition in mechanism (from subcritical crack growth to pressure solution-dominated creep) at $P_{eff} = 10$ MPa and at $P_{eff} = 20$ MPa would be more marked than currently predicted by our simple approach if coupled effects were accounted for.

The very heterogenous microstructure of Purbeck limestone (and of grainstones in general) is very likely to manifest itself through spatially heterogeneous deformation mechanisms, with subcritical crack growth occurring in the cement, at the same time as pressure solution or ductile granular flow occurs within the microporous peloids. In that context, even a modest change in stress conditions can change the relative amount of deformation and deformation rate accommodated in the cement as against the peloids. Hence, the change in behavior observed at low strain rates at $P_{eff} = 20$ MPa might correspond to a temporary switch in the partitioning of strain between the brittle cement and the ductile peloids. In that regard, the interconnection of the peloids around the cement is crucial for the development of large strains. Of course, the strain compatibility conditions at the interface between cement and peloids, and the lack of active intracrystalline plastic deformation mechanisms in the coarse grained cement, make crack growth

in the cement inevitable. Thus, the ductile, compactant deformation behavior at low strain rate is expected to be only temporary. This is consistent with the results of the creep experiments performed at the lowest stresses (Figure 8), during which deformation accelerates after a sustained period of stable creep: the high strain rate reached during tertiary creep would eventually bring the deformation back into the crack growth-dominated regime.

6.3. Implications for the Deformation of the Crust

Our experimental results indicate that, under shallow crustal conditions, limestone deformation is controlled by two possible rate-dependent mechanisms: subcritical crack growth and pressure solution. While the former mechanism is fundamentally dilatant and leads to macroscopic failure, the latter is compactant and leads to stable creep. The switch in mechanism is controlled by the applied stress and/or strain rate.

This has some important implications for the architecture of faults cutting carbonate sequences [e.g., *Tesei et al.*, 2013] and more generally for the deformation of the crust around fault zones throughout the seismic cycle. During the post seismic phase, faults generally undergo decelerating afterslip [e.g., *Scholz*, 2002], and the whole fault zone relaxes. In a fault hosted in porous limestone, we would expect that the deformation immediately following an earthquake would be dominated by subcritical crack growth, whereas pressure solution creep would likely dominate the later stages. This in turn has implications for fluid flow in and around the fault zone [*Gratier*, 2011]: the dilatant cracking induced by the earthquake and during the subsequent crack growth-driven creep stage will tend to increase the permeability of the fault rocks, accelerate fluid flow, and reequilibrate pore pressure. By contrast, the ensuing stage of pressure solution-driven creep will tend to seal the fault during deformation and isolate the pore space of the fault rocks from the surrounding country rocks [*Gratier*, 2011].

The occurrence of two competing deformation mechanisms in porous limestone also impacts our ability to make predictions of reservoir deformation during oil production of fluid (e.g., CO_2) injection. A practical implication of our results is that a porous limestone undergoing creep (for instance due to a pore fluid withdrawal in an oil field or near a borehole) can either deform in a stable manner (if pressure solution is the dominant mechanism) or accelerate until failure (if subcritical cracking is the dominant mechanism); the long-term stability of the rock depends crucially on the local stress level. One critical difference between the two deformation mechanisms is that subcritical crack growth alone is not expected to allow large strains (only of the order of a few percent in the brittle regime explored in our experiments), whereas pressure solution can accommodate much larger strains (up to several tens of percent) [*Gratier et al.*, 2013]. The identification and monitoring of accelerating or decelerating trends in the deformation rates, as well as the estimation of total accumulated strain, may help to determine the dominant deformation mechanism and hence improve the predictability of time-dependent rock failure in reservoirs.

7. Conclusions

We performed triaxial deformation experiments on a porous limestone under water-saturated conditions. At $P_{eff} = 10$ MPa, the samples are brittle and the time-dependent brittle behavior is very similar to that of porous sandstones. The phenomenon of brittle creep occurs and is characterized by the same features as in other rock types: a primary, decelerating creep stage, followed by an inflection and a tertiary (accelerating) creep stage; concomitantly, *P* wave speeds measured in all orientations throughout the sample decrease continuously, indicating an increase in crack density. At $P_{eff} = 20$ MPa, the rock is still brittle, and brittle creep also occurs. However, the details of the time-dependent, brittle creep behavior are different from those observed at $P_{eff} = 10$ MPa. First, the total deformation accumulated before failure during brittle creep dramatically increases with decreasing creep strain rate. Second, the decrease in *P* wave speed with increasing deformation becomes less marked when strain rate is lower. Third, additional strain rate-stepping experiments indicate that the deformation is more compactant at low strain rates. Taken together, these observations suggest that an additional deformation mechanism becomes active at low strain rates.

The observed time-dependent behavior at $P_{eff} = 20$ MPa can be explained by a combination of mechanisms: enhanced plastic flow at microcrack tips and pressure solution within the peloids.

The intricate microstructure, together with the complexity of the deformation mechanisms of calcite, makes microphysical modeling of the rate-dependent deformation processes in porous limestone very

challenging. However, the work presented here, for example, in the form of the deformation mechanism maps, does provide an initial framework for determining where future efforts should be concentrated.

Acknowledgments
The authors are grateful to Ian Wood for X-ray diffraction analysis of the rock, to Neil Hughes and Steve Boon for their help during experimentation at UCL, and to Thierry Reuschlé for setting up the triaxial apparatus in Strasbourg. Thanks also to Chris Spiers for clarifying the use of pressure solution creep laws and to him and Jean-Pierre Gratier for their very useful review comments. This work was supported by the Natural Environment Research Council (grants NE/G016909/1 and NE/K009656/1) and CNRS PICS grant 5993. The data for this paper are available from the authors upon request.

References

Ayling, M. R., P. G. Meredith, and S. A. F. Murrell (1995), Microcracking during triaxial deformation of porous rocks monitored by changes in rock physical properties. I. Elastic-wave propagation measurements on dry rocks, *Tectonophysics*, *245*, 205–221.

Baker, P. A., M. Kastner, J. D. Byerlee, and D. A. Lockner (1980), Pressure solution and hydrothermal recrystallization of carbonate sediments—An experimental study, *Mar. Geol.*, *38*(1-3), 185–203.

Bastesen, E., A. Braathen, H. Nottveit, R. H. Gabrielsen, and T. Skar (2009), Extensional fault cores in micritic carbonate—Case studies from the Gulf of Corinth, Greece, *J. Struct. Geol.*, *31*(4), 403–420.

Baud, P., and P. G. Meredith (1997), Damage accumulation during triaxial creep of Darley Dale sandstone from pore volumometry and acoustic emission, *Int. J. Rock Mech. Min. Sci.*, *34*(3-4), 368.

Baud, P., A. Schubnel, and T.-F. Wong (2000), Dilatancy, compaction, and failure mode in Solnhofen limestone, *J. Geophys. Res.*, *105*(B8), 19,289–19,303.

Baud, P., S. Vinciguerra, C. David, A. Cavallo, E. Walker, and T. Reuschlé (2009), Compaction and failure in high porosity carbonates: Mechanical data and microstructural observations, *Pure Appl. Geophys.*, *166*, 869–898.

Brantut, N., A. Schubnel, and Y. Guéguen (2011), Damage and rupture dynamics at the brittle-ductile transition: The case of gypsum, *J. Geophys. Res.*, *116*, B01404, doi:10.1029/2010JB007675.

Brantut, N., P. Baud, M. J. Heap, and P. G. Meredith (2012), Micromechanics of brittle creep in rocks, *J. Geophys. Res.*, *117*, B08412, doi:10.1029/2012JB009299.

Brantut, N., M. J. Heap, P. G. Meredith, and P. Baud (2013), Time-dependent cracking and brittle creep in crustal rocks: A review, *J. Struct. Geol.*, *52*, 17–43.

Brantut, N., M. J. Heap, P. Baud, and P. G. Meredith (2014), Rate- and strain-dependent brittle deformation of rocks, *J. Geophys. Res. Solid Earth*, *119*, 1818–1836, doi:10.1002/2013JB010448.

Cilona, A., P. Baud, E. Tondi, F. Agosta, S. Vinciguerra, A. Rustichelli, and C. J. Spiers (2012), Deformation bands in porous carbonate grainstones: Field and laboratory observations, *J. Struct. Geol.*, *45*, 137–157.

Croizé, D., K. Bjørlykke, J. Jahren, and F. Renard (2010), Experimental and chemical compaction of carbonate sand, *J. Geophys. Res.*, *115*, B11204, doi:10.1029/2010JB007697.

Croizé, D., F. Renard, and J.-P. Gratier (2013), Compaction and porosity reduction in carbonates: A review of observations, theory and experiments, in *Advances in Geophysics*, vol. 54, edited by R. Dmowska, pp. 181–238, Elsevier, San Diego, Calif.

Darot, M., and Y. Guéguen (1986), Slow crack growth in minerals and rocks: Theory and experiments, *Pure Appl. Geophys.*, *124*(4/5), 677–692.

Dautriat, J., N. Gland, A. Dimanov, and J. Raphanel (2011), Hydromechanical behavior of heterogeneous carbonate rock under proportional triaxial loadings, *J. Geophys. Res.*, *116*, B01205, doi:10.1029/2009JB000830.

de Bresser, J. H. P., and C. J. Spiers (1993), Slip systems in calcite single crystals deformed at 300–800°C, *J. Geophys. Res.*, *98*(B4), 6397–6409.

Duda, M., and J. Renner (2013), The weakening effect of water on the brittle failure strength of sandstone, *Geophys. J. Int.*, *192*, 1091–1108.

Fischer, G. J., and M. S. Paterson (1992), Measurement of permeability and storage capacity in rocks during deformation at high temperature and pressure, in *Fault Mechanics and Transport Properties of Rocks, Int. Geophys. Ser.*, edited by B. Evans, and T. F. Wong, pp. 187–211, Academic Press, London, U. K.

Ford, D., and P. Williams (2007), *Karst Hydrogeology and Geomorphology*, John Wiley, Chichester, U. K.

Fredrich, J. T., B. Evans, and T.-F. Wong (1989), Micromechanics of the brittle to plastic transition in Carrara marble, *J. Geophys. Res.*, *94*, 4129–4145.

Gratier, J.-P. (2011), Fault permeability and strength evolution related to fracturing and healing episodic processes (years to millennia): The role of pressure solution, *Oil Gas Sci. Technol. – Rev. IFP Energies nouvelles*, *66*(3), 491–506, doi:10.2516/ogst/2010014.

Gratier, J.-P., and J.-F. Gamond (1990), Transition between seismic and aseismic deformation in the upper crust, in *Deformation Mechanisms, Rheology and Tectonics, Special Publications*, vol. 54, edited by R. J. Knipe and E. H. Rutter, pp. 461–473, Geol. Soc., London.

Gratier, J.-P., F. Renard, and P. Labaume (1999), How pressure solution creep and fracturing processes interact in the upper crust to make it behave in both a brittle and viscous manner, *J. Struct. Geol.*, *21*, 1189–1197.

Gratier, J.-P., D. K. Dysthe, and F. Renard (2013), The role of pressure solution creep in the ductility of the Earth's upper crust, in *Advances in Geophysics*, vol. 54, edited by R. Dmowska, pp. 47–179, Elsevier, San Diego, Calif.

Guéguen, Y., and M. Kachanov (2011), Effective elastic properties of cracked and porous rocks—An overview, in *Mechanics of Crustal Rocks*, edited by Y. M. Leroy and F. K. Lehner, pp. 73–125, Springer, Berlin Heidelberg, Germany.

Heap, M. J., P. Baud, P. G. Meredith, A. F. Bell, and I. G. Main (2009), Time-dependent brittle creep in Darley Dale sandstone, *J. Geophys. Res.*, *114*, B07203, doi:10.1029/2008JB006212.

Heap, M. J., P. Baud, P. G. Meredith, S. Vinciguerra, A. F. Bell, and I. G. Main (2011), Brittle creep in basalt and its application to time-dependent volcano deformation, *Earth Planet. Sci. Lett.*, *307*, 71–82.

Hellman, R., P. J. N. Renders, J.-P. Gratier, and R. Guiguet (2002), Experimental pressure solution compaction of chalk in aqueous solutions. Part 1. Deformation behavior and chemistry, in *Water-Rock Interactions, Ore Deposits, and Environmental Geochemistry: A Tribute to David A. Crerar*, vol. 7, edited by R. Hellmann and S. A. Wood, pp. 129–152, Special Publication, Geochemical Society, St. Louis, Mo.

Inskeep, W. P., and P. R. Bloom (1985), An evaluation of rate equations for calcite precipitation kinetics at pCO_2 less than 0.01 atm and pH greater than 8, *Geochim. Cosmochim. Acta*, *9*, 2165–2180.

Kranz, R. L., and C. H. Scholz (1977), Critical dilatant volume of rocks at the onset of tertiary creep, *J. Geophys. Res.*, *82*(30), 4893–4898.

Lawn, B. R. (1993), *Fracture of Brittle Solids,* 2nd ed., Cambridge Univ. Press, Cambridge, U. K.

Lehner, F. K. (1990), Thermodynamics of rock deformation by pressure solution, in *Deformation Processes in Minerals, Ceramics and Rocks*, edited by D. J. Barber and P. G. Meredith, pp. 296–333, Unwin Hayman, London, U. K.

Linzer, H.-G., L. Ratschbacher, and W. Frisch (1995), Transpressional collision structures in the upper crust: The fold-thrust belt of the northern calcareous Alps, *Tectonophysics*, *242*(1-2), 41–61.

Nakashima, S. (1995), Diffusivity of ions in pore water as a quantitative basis for rock deformation rate estimates, *Tectonophysics*, *245*(3-4), 185–203.

Paterson, M. S., and T. F. Wong (2005), *Experimental Rock Deformation—The Brittle Field,* 2nd ed., Springer-Verlag, Berlin Heidelberg, Germany.

Plummer, L. N., and E. Busenberg (1982), The solubilities of calcite, aragonite and vaterite in CO_2-H_2O solutions between 0 and s 90°C, and an evaluation of the aqueous model for the system $CaCO_3$-CO_2-H_2O, *Geochim. Cosmochim. Acta*, *46*(6), 1011–1040.

Renard, F., P. Ortoleva, and J.-P. Gratier (1997), Pressure solution in sandstones: Influence of clays and dependence on temperature and stress, *Tectonophysics*, *280*(3), 257–266.

Rowe, K. J., and E. H. Rutter (1990), Palaeostress estimation using calcite twinning: Experimental calibration and application to nature, *J. Struct. Geol.*, *12*(1), 1–17.

Røyne, A., J. Bisschop, and D. K. Dysthe (2011), Experimental investigation of surface energy and subcritical crack growth in calcite, *J. Geophys. Res.*, *116*, B04204, doi:10.1029/2010JB008033.

Rutter, E. H. (1972), The effects of strain-rate changes on the strength and ductility of Solnhofen limestone at low temperatures and confining pressures, *Int. J. Rock Mech. Min. Sci.*, *9*, 183–189.

Scholz, C. H. (2002), *The Mechanics of Earthquake and Faulting,* 2nd ed., Cambridge Univ. Press, Cambridge, U. K.

Tesei, T., C. Collettini, C. Viti, and M. R. Barchi (2013), Fault architecture and deformation mechanisms in exhumed analogues of seismogenic carbonate-bearing thrusts, *J. Struct. Geol.*, *55*, 167–181.

Turner, F. J., D. T. Griggs, and H. Heard (1954), Experimental deformation of calcite crystals, *Geol. Soc. Am. Bull.*, *65*(9), 883–934.

Vajdova, V., P. Baud, and T.-F. Wong (2004), Compaction, dilatancy, and failure in porous carbonate rocks, *J. Geophys. Res.*, *109*, B05204, doi:10.1029/2003JB002508.

Vajdova, V., P. Baud, L. Wu, and T.-F. Wong (2012), Micromechanics of inelastic compaction in two allochemical limestones, *J. Struct. Geol.*, *43*, 100–117.

Wong, T.-F., and P. Baud (2012), The brittle-ductile transition in porous rock: A review, *J. Struct. Geol.*, *44*, 25–53.

Zhang, X., and C. J. Spiers (2005), Compaction of granular calcite by pressure solution at room temperature and effects of pore fluid chemistry, *Int. J. Rock Mech. Min. Sci.*, *42*, 950–960.

Zhang, X., C. J. Spiers, and C. J. Peach (2010), Compaction creep of wet granular calcite by pressure solution at 28°C to 150°C, *J. Geophys. Res.*, *115*, B09217, doi:10.1029/2008JB005853.

Zhu, W., P. Baud, and T.-F. Wong (2010), Micromechanics of cataclastic pore collapse in limestone, *J. Geophys. Res.*, *115*, B04405, doi:10.1029/2009JB006610.